Journal of Loss Prevention in the Process Industries 76 (2022) 104755

Contents lists available at ScienceDirect

Journal of Loss Prevention in the Process Industries

journal homepage: www.elsevier.com/locate/jlp

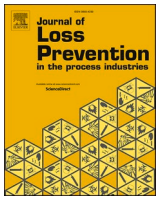

CFD simulation of turbulent fluid flow and dust dispersion in the 1 m^3 explosion vessel equipped with the rebound nozzle

Maria Portarapillo [a,*], Marco Trofa [a], Roberto Sanchirico [b], Almerinda Di Benedetto [a]

[a] Department of Chemical, Materials and Production Engineering, University of Naples Federico II, Naples, 80125, Italy
[b] Istituto di Scienze e Tecnologie per l'Energia e la Mobilità Sostenibili STEMS-CNR, Naples, 80125, Italy

ARTICLE INFO

Keywords:
CFD simulation
Dust dispersion
Rebound nozzle
Perforated annular nozzle
1 m^3 vessel

ABSTRACT

Against dust explosions, all the flammability and explosibility parameters must be evaluated following standard procedures using the 20 L and/or the 1 m^3 vessel. Previous results comparing the dust dispersion in the 20 L sphere equipped with rebound or perforated annular nozzle showed that the initial turbulence level, the dust concentration, and the feeding are affected by the type of nozzle used. In this work, a similar investigation was performed on the 1 m^3 vessel, simulating the fluid flow evolution which is obtained with the rebound nozzle. Results showed that the 1 m^3 vessel equipped with rebound nozzle presents a less uniform degree of turbulence and a higher amount of dust fed, compared to the case of perforated annular nozzle. However, the greatest effect on the initial level of turbulence and turbulent combustion regime is determined by the size of the vessel and not by the type of nozzle used.

1. Introduction

Dust explosions can have destructive impacts on lives, properties, and the environment. In any industry where fine particulate combustible material is handled, stored, or produced, explosion may occur. To lessen hazards, and consequently the risk, and mitigate the potential consequences of a totally or partially confined dust deflagration, prevention (i.e., ignition source control, elimination or adequate reduction of fuel, oxygen concentration reduction) and protection/mitigation (i.e., pressure containment, venting) measures have to be *ad hoc* designed. To this aim, the explosibility and flammability parameters assessment is required. Most of these parameters (minimum explosible concentration, MEC; limiting oxygen concentration, LOC; maximum explosion pressure, P_{max}; and deflagration index, K_{St}) are evaluated in 20 L and/or 1 m^3 vessels, according to standard procedures (ASTM E1226-19, 2019; ASTM E1515-14, 1993; ASTM E2931-13, 2013; ISO 6184-1:1985, 1985; UNI EN 14034-(1–4), 2011). A great deal of effort has been devoted to identifying the conditions in which the results obtained in both vessels agree. Unfortunately, significant discrepancies have been found between the results obtained with the 20 L sphere and the 1 m^3 vessel once dusts different from standard ones have been tested (Cashdollar and Chatrathi, 1992; Clouthier et al., 2019; Going et al., 2000; Proust et al., 2007; Rodgers and Ural, 2011; Taveau et al., 2018, 2019). To properly design prevention and mitigation measures, the measurements carried out in these standard vessels for a fixed powder must be equivalent (once the calibration procedure has been carried out), reliable, and repeatable. Noteworthy, the pre-ignition turbulence and the dust concentration distribution within the vessel play a major role in affecting the unsteady flame propagation and then explosion/flammability parameters. Particularly, the control of the turbulence level in both vessels is of crucial importance. Such conditions are affected not only by the design and the size of the test vessels but also by the dust properties like particle density, diameter, and shape.

In the years, experimental measurements of turbulence and dust concentration have been carried out (Dyduch et al., 2016; Hauert and Vogl, 1995; Kalejaiye et al., 2010). However, these measurements allow the evaluation of these properties only in few points of the vessels.

Therefore, to get insights into the spatial/temporal maps of fluid flow and dust concentration, established inside the 20 L and the 1 m^3 vessels, CFD models have been developed and validated (Di Benedetto et al., 2013; Portarapillo et al., 2020b). Results showed that the turbulent fluid flow and the dust distribution are not uniform and that they strongly depend on the dust properties (Portarapillo et al., 2020a, 2021b). Recently, we showed that at the recommended ignition delay time (i.e., (60 ± 5) ms in the 20 L vessel and (600 ± 100) ms in the 1 m^3 vessel), the fluid flow features established in the 20 L and in the 1 m^3 vessels are

* Corresponding author.
E-mail address: maria.portarapillo@unina.it (M. Portarapillo).

https://doi.org/10.1016/j.jlp.2022.104755
Received 21 June 2021; Received in revised form 8 February 2022; Accepted 18 February 2022
Available online 21 February 2022
0950-4230/© 2022 Elsevier Ltd. All rights reserved.

significantly different. In particular, in the 20 L vessel, the turbulent kinetic energy is always higher and rather not uniform compared to that of 1 m^3 vessel (Portarapillo et al., 2020b). In a recent work, we concluded that the differences between the explosion tests in the 20 L and 1 m^3 vessels are qualitative other than quantitative, being different not only the turbulent kinetic energy but also the turbulent combustion regime, which significantly affects the flame propagation mode and eventually the explosion severity. In the 1 m^3 vessel, the quasi-steady corrugated flamelets regime is established. Conversely, the higher turbulence level in the 20 L sphere increases the transport within the preheating region and leads to a higher volumetric heat release and shorter combustion times (thin reaction zone regime), whatever the nozzle used (Portarapillo et al., 2021a).

Another important parameter which strongly affects the fluid flow spatial/temporal evolution inside the explosion vessel is the nozzle design. The effect of the nozzle was investigated by means of CFD models in the 20 L test vessel (Di Benedetto et al., 2013; Di Sarli et al., 2015). Simulation results showed that when the 20 L vessel is equipped with the perforated annular nozzle, the turbulence level is lower and the flow field is more homogeneous than in the case with the rebound nozzle.

In the standards, the nozzles are presented as interchangeable alternatives, without highlighting any kind of difference. In particular, in the standard procedure for the 1 m^3 dust explosion vessel the rebound nozzle is suggested as an alternative in the case of fibrous dusts testing (ASTM E1226-19, 2019; UNI EN 14034-(1–4), 2011). However, due to the partial feeding obtained with the perforated annular nozzle, the rebound nozzle is the most currently used during the explosion testing. The turbulence and dust mass concentration temporal/spatial evolution can significantly change when the rebound nozzle is used. In this work, we aim at simulating the dust dispersion inside the 1 m^3 vessel equipped with the rebound nozzle, when injecting either only air or dust-air mixtures. The simulation results allow getting insights into the fluid flow evolution established inside the vessel equipped with the rebound nozzle. The comparison with the 1 m^3 vessel equipped with the perforated annular nozzle could suggest the best operating conditions for keeping under control the explosion/flammability tests.

2. Model description

2.1. 1 m^3 equipment for dust explosion testing equipped with rebound nozzle

In this work, CFD simulations of the dust dispersion in the standard 1 m^3 vessel apparatus were run (ISO 6184-1:1985, 1985; UNI EN 14034-(1–4), 2011). The equipment mainly consists of a spherical vessel of 1 m^3 and a dust container (5.4 L), closed by a fast-acting valve. The connecting tube between the fast-acting valve and the dust container must be no longer than 350 mm, as suggested in the standards (ISO 6184-1:1985, 1985; UNI EN 14034-(1–4), 2011). The container with the required amount of dust is pressurised to 21 bar while the vessel is left at ambient pressure. For dispersing the dust inside the vessel, a rebound nozzle is mounted inside the explosion vessel. The rebound nozzle was built following the drawing dimensions reported in UNI EN 14034–2 and UNI EN 14034–3 (UNI EN 14034-(1–4), 2011) (Fig. 1). Noteworthy, discrepancies were found in those reported in UNI EN 14034–1, UNI EN 14034–4 and BS EN 14034–1 (BS EN 14034–1, 2004; UNI EN 14034-(1–4), 2011). The ignition delay time (i.e., the duration of the dust dispersion) was set at (600 ± 100) ms. CFD simulations of the vessel equipped with perforated annular nozzle were computed for the sake of comparison. The CFD model for this equipment was presented and validated in previous studies (Portarapillo et al., 2020b; 2021a; 2021b).

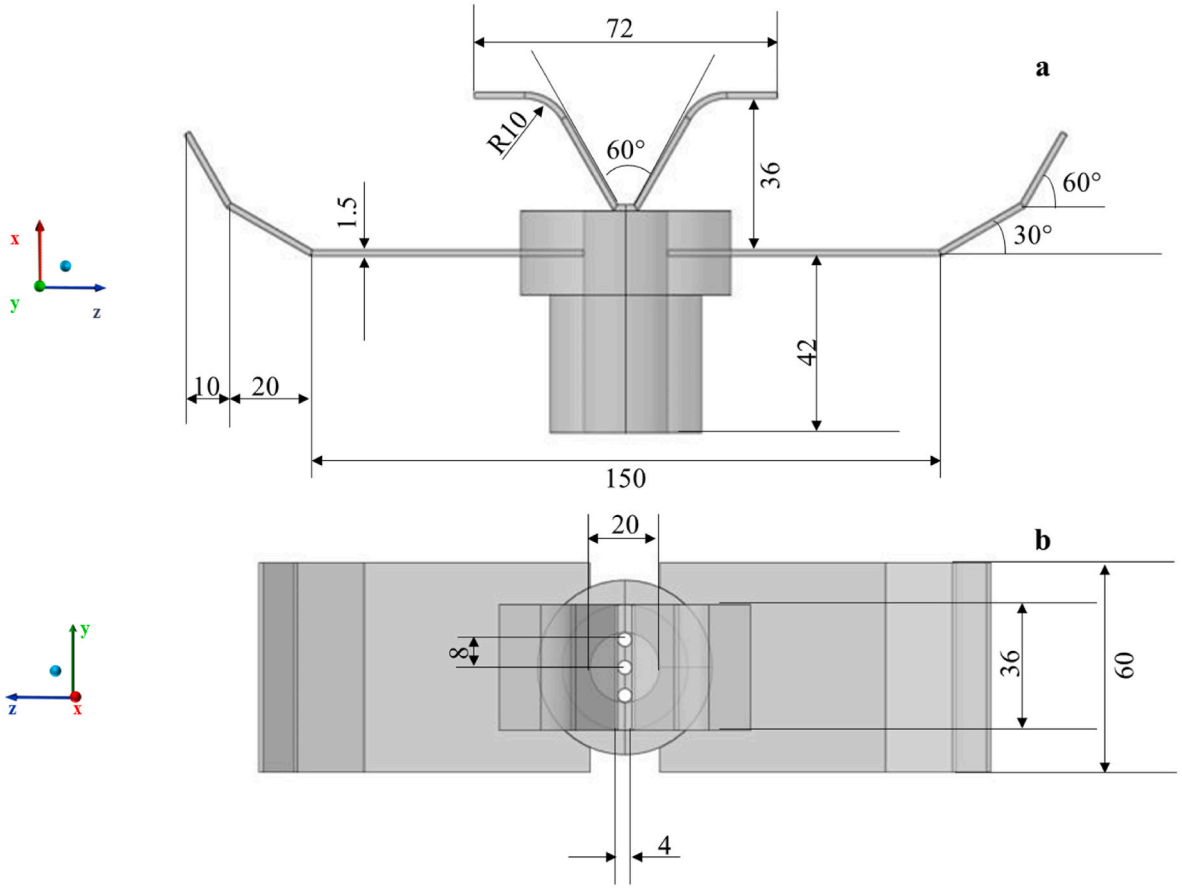

Fig. 1. Front (a) and top (b) view of the rebound nozzle used in 1 m^3 vessel.

2.2. CFD model

The computational domain and mesh of 1 m^3 vessel were built and refined by means of the Design Modeler and Meshing packages of Ansys (Release 2020 R2). In Table 1, geometrical details of the computational domain are provided. A section of the used unstructured mesh and a zoom close to the rebound are shown in Fig. 2.

The continuum phase is modelled through the Reynolds-averaged Navier-Stokes equations (Eulerian approach). The continuity and momentum balance equations are

$$\frac{\partial \rho}{\partial t} + \nabla \cdot (\rho \boldsymbol{u}) = 0 \tag{1}$$

$$\frac{\partial (\rho \boldsymbol{u})}{\partial t} + \nabla \cdot (\rho \boldsymbol{u}\boldsymbol{u}) = -\nabla p + \nabla \cdot \boldsymbol{\tau} + \rho \boldsymbol{g} + \boldsymbol{F} \tag{2}$$

where ρ (kg/m^3) is the fluid density, $\boldsymbol{u}$ (m/s) is the fluid velocity vector, p (Pa) is the static pressure, $\boldsymbol{\tau}$ (Pa) is the stress tensor, $\boldsymbol{g}$ (m/s^2) is the gravity vector, and $\boldsymbol{F}$ (N) is the momentum exchange term due to the presence of the suspended particles. These were solved using the standard k-ε model with standard wall function and considering compressibility effects (Launder and Spalding, 1972). The fluid flow equations were finite-volume discretized on the 3D tetrahedral unstructured grid (506805 elements), refined in correspondence of the rebound, along the feeding tube, and in the dust container (as shown in Fig. 2). More precisely, we created specific lines for the mesh construction at the middle of the feeding tube, close to the rebound and on the dust container edge and we set a number of elements along them. In general, we had a maximum size of the elements of about 10 mm and a growth rate at 1.15. The semi-implicit method for pressure-linked equations (SIMPLE) was used to solve the pressure-velocity coupled equations. First order schemes for convective terms and second order schemes for diffusion terms were used for the spatial discretization of the model equations. First-order scheme was used to discretize temporal derivatives (time step of 4×10^{-5} s).

The flow of the dust was solved with the Lagrangian formulation using the Discrete Phase Model (DPM). The force balance on each particle reads as follows (Fluent Inc, 2016):

$$\frac{d\boldsymbol{u}_p}{dt} = \boldsymbol{f}_D + \frac{\boldsymbol{g}(\rho_p - \rho)}{\rho_p} + \boldsymbol{f} \tag{3}$$

with $\boldsymbol{u}_p$ (m/s) the particle velocity, ρ_p (kg/m^3) the particle density, $\boldsymbol{f}_D$ (N/kg) the drag force per unit particle mass, and $\boldsymbol{f}$ (N/kg) which incorporates all the additional forces acting on the particle. The drag force is a function of the particle Reynolds number Re and of the drag coefficient C_D according to the following equations:

$$\boldsymbol{f}_D = \frac{18\mu}{\rho_p d_p^2} \frac{C_D \mathrm{Re}}{24} (\boldsymbol{u} - \boldsymbol{u}_p) \tag{4}$$

$$\mathrm{Re} = \frac{\rho d_p |\boldsymbol{u}_p - \boldsymbol{u}|}{\mu} \tag{5}$$

$$C_D = a_1 + \frac{a_2}{\mathrm{Re}} + \frac{a_3}{\mathrm{Re}^2} \tag{6}$$

where μ (Pa•s) is the fluid viscosity, d_p (m) is the particle diameter, and

Table 1
– Geometrical details of the computational domain.

Geometrical detail	Value
Container volume (m^3)	0.0054
Tube diameter (m)	0.02
Tube length (m)	0.35
Sphere volume (m^3)	1

where a_1, a_2 and a_3 (−) are constants given by Morsi and Alexander (1972) (Morsi and Alexander, 1972) for smooth spherical particles.

Equation (3) incorporates additional forces $\boldsymbol{f}$ per unit particle mass. Among these, the most important ones are the "virtual mass" force, i.e., the force required to accelerate the fluid surrounding the particle

$$\boldsymbol{f} = 0.5 \frac{\rho}{\rho_p} \left(\boldsymbol{u}_p \cdot \nabla \boldsymbol{u} - \frac{d\boldsymbol{u}_p}{dt} \right) \tag{7}$$

and the pressure gradient force

$$\boldsymbol{f} = \frac{\rho}{\rho_p} \boldsymbol{u} \cdot \nabla \boldsymbol{u} \tag{8}$$

The turbulent dispersion was considered activating the Discrete Random Walk (DRW) model. In this way, the interaction of a particle with a succession of discrete fluid phase turbulent eddies is simulated (Fluent Inc, 2016). The DPM model can be implemented when the second phase is dilute (i.e., volume fraction lower than 10–12%) enough to apply the two-way coupling approach (Elghobashi, 1994). In this work, the solid fraction was equal to $\alpha = 4.9 \times 10^{-5}$.

The unsteady particle tracking time step was taken equal to the fluid flow time step. Parallel calculations were performed through the segregated pressure-based solver of the code ANSYS Fluent (Release 2020 R2). All residuals were set equal to 10^{-6} for convergence purpose. The fluid phase was air at atmospheric temperature and was modelled as an ideal gas.

As boundary conditions, we set the no-slip condition and zero roughness for the continuum, the heat flow equal to zero (adiabatic case), and the reflection for the discrete phase. As initial conditions, we adopted that used in the standard tests: the dust container was initially at pressure equal to 21 bar while the connecting tube and the sphere were set to 1 bar. Computations were performed for a dust with a diameter equal 250 μm. Comparison with the previous results obtained with the perforated annular nozzle is also performed (Portarapillo et al., 2020b). The simulation conditions for both standard nozzles are summarised in Table 2.

3. Results

3.1. CFD model validation

Fig. 3 shows the temporal trend of pressure as computed in the centre of the dust container, in the case of dust-free air and dust at C = 100 g/m^3. As exhibited by the pressure trends, the feeding phase lasts 0.4 s in which the dust container reaches 1 bar and the injection of air/dust-air comes to an end. The pressure trend was compared to experimental data available in the literature to validate the CFD model (Dyduch et al., 2016). Dyduch et al. (2016) measured the pressure trend and the transient flow velocity generated by air outflow from the dust dispersion system inside the standard 1 m^3 vessel equipped with the rebound nozzle. The comparison shows a very good agreement.

In Fig. 4 the root mean square velocity (u_{RMS}) temporal trend in the case of dust-free air and dust at a concentration equal to 100 g/m^3 are shown as computed in the centre of the sphere. The RMS velocity was calculated from the turbulent kinetic energy by considering isotropic flow field. For the sake of comparison, the experimental data measured by Dyduch et al. (2016) are also shown (Dyduch et al., 2016). The comparison shows a good agreement starting from 0.3 s.

3.2. TKE maps and dust distribution

In Fig. 5 the time sequence of the turbulent kinetic energy maps is shown as computed over the frontal (x-z) plane in case of dust-free air (a) and dust at 100 g/m^3 (b). At 400 ms and 600 ms, the maps with dust present non-symmetric fields, differently from the results obtained in the case of dust-free air. The occurrence of an asymmetric flow is

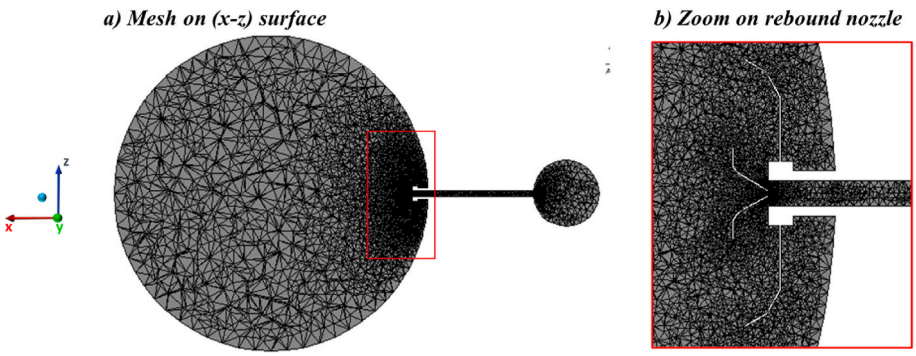

Fig. 2. Section of the unstructured and nonuniform mesh used, (x–z) central plane (a) and zoom on rebound nozzle zone (b).

Table 2
Simulation conditions.

	1 m^3 sphere
Initial pressure of container (bar)	21
Initial pressure of sphere and container (bar)	1
Dust concentration (g/m^3)	100
Dust density (kg/m^3)	2046
Dust diameter (μm)	250
Time step (s)	4×10^{-5}
Number of time steps	15000

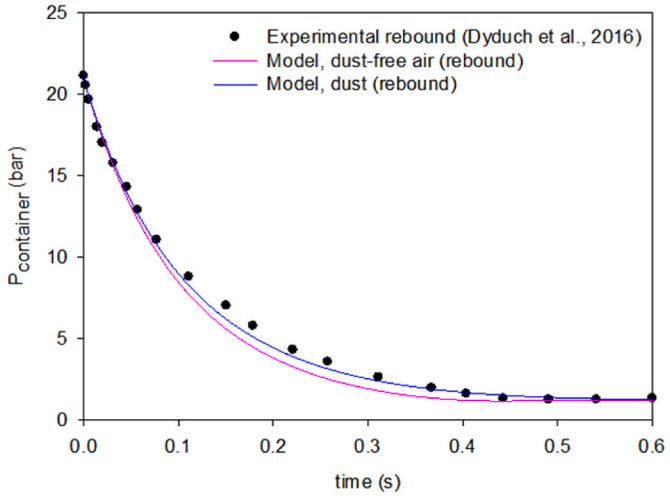

Fig. 3. – *Pressure time histories computed in the centre of the dust container for dust-free air (pink line) and dust-air mixture (blue line). Literature data are also shown for the sake of comparison (black scatter plot)* (Dyduch et al., 2016). (For interpretation of the references to colour in this figure legend, the reader is referred to the Web version of this article.)

determined by the action of gravity on the dispersed phase. Kartushinsky et al. (2011) developed a three-dimensional model of particulate flow in a horizontal pipe using the Reynolds Averaged Navier-Stokes method, showing that in spite of the geometric symmetry, the presence of solid particles in the flow may produce asymmetric fields due to gravity and particle sedimentation. The flow asymmetry cannot be accounted for with two-dimensional models (Kartushinsky et al., 2011). Moreover, in our previous papers, we showed that in both the 20 L spherical vessel and in the 1 m^3 vessel, a non-symmetric flow may establish in the presence of dust particles (Di Benedetto et al., 2013; Portarapillo et al., 2020b). Although the level of turbulence is not completely uniform within the sphere at 600 ms, showing a decay moving from the centre to the walls, the variation range of turbulent kinetic energy is very narrow (from 4.5 m^2/s^2 to 0 m^2/s^2).

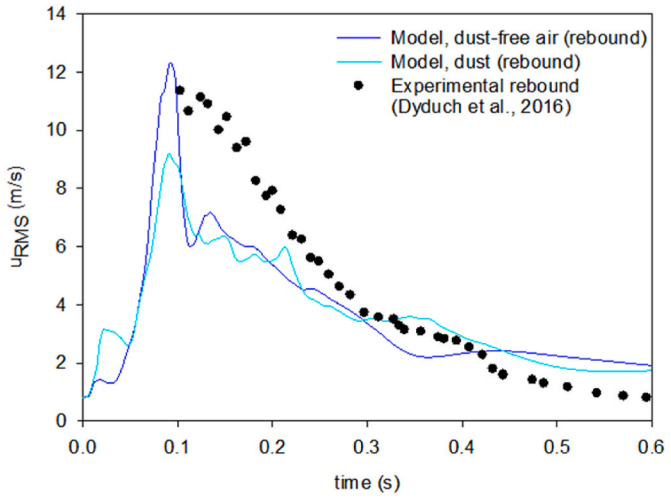

Fig. 4. – *RMS turbulence velocity (m/s) as a function of the time at the centre of the 1 m^3 vessel for dust free air (blue line) and dust-air mixture (cyan lines). Literature data are also shown for the sake of comparison (black scatter plot)* (Dyduch et al., 2016). (For interpretation of the references to colour in this figure legend, the reader is referred to the Web version of this article.)

Fig. 6 shows the spatial-temporal distribution of the dust concentration inside the sphere represented through the ratio χ between the dust concentration and the nominal dust concentration (C = 100 g/m^3) as obtained on the (x-z) plane (a) and in the whole sphere (b) oriented as in the empty image. The highest dust concentrations are attained on the vortex's edges. Dust is highly concentrated at the sphere walls and in the centre, reaching concentrations much higher than the nominal value (χ = 2; C = 200 g/m^3), while in the bulk of the sphere, the dust concentration is lower than the nominal value (χ < 1; C < 100 g/m^3). On increasing time, dust particles start to settle, increasing the amount of particles at the bottom walls. At 600 ms, the highest concentration of particles was obtained at the bottom of the sphere due to the gravity effect, acting in the negative z-direction. This result is in agreement with the findings by Kalejaiye et al. (2010). In their work, lower values of transmission (and then higher values of concentration) were found in correspondence to the probes close to the vessel walls with respect to those closer to the sphere centre (Kalejaiye et al., 2010).

3.3. Comparison between perforated annular and rebound nozzles

As stated before, in the standard procedures the annular and rebound nozzles are presented as interchangeable alternatives. For example, in the standard for the 1 m^3 dust explosion vessel, the rebound nozzle is deemed as a suitable alternative in the case of fibrous dusts testing (ASTM E1226-19, 2019; UNI EN 14034-(1–4), 2011).

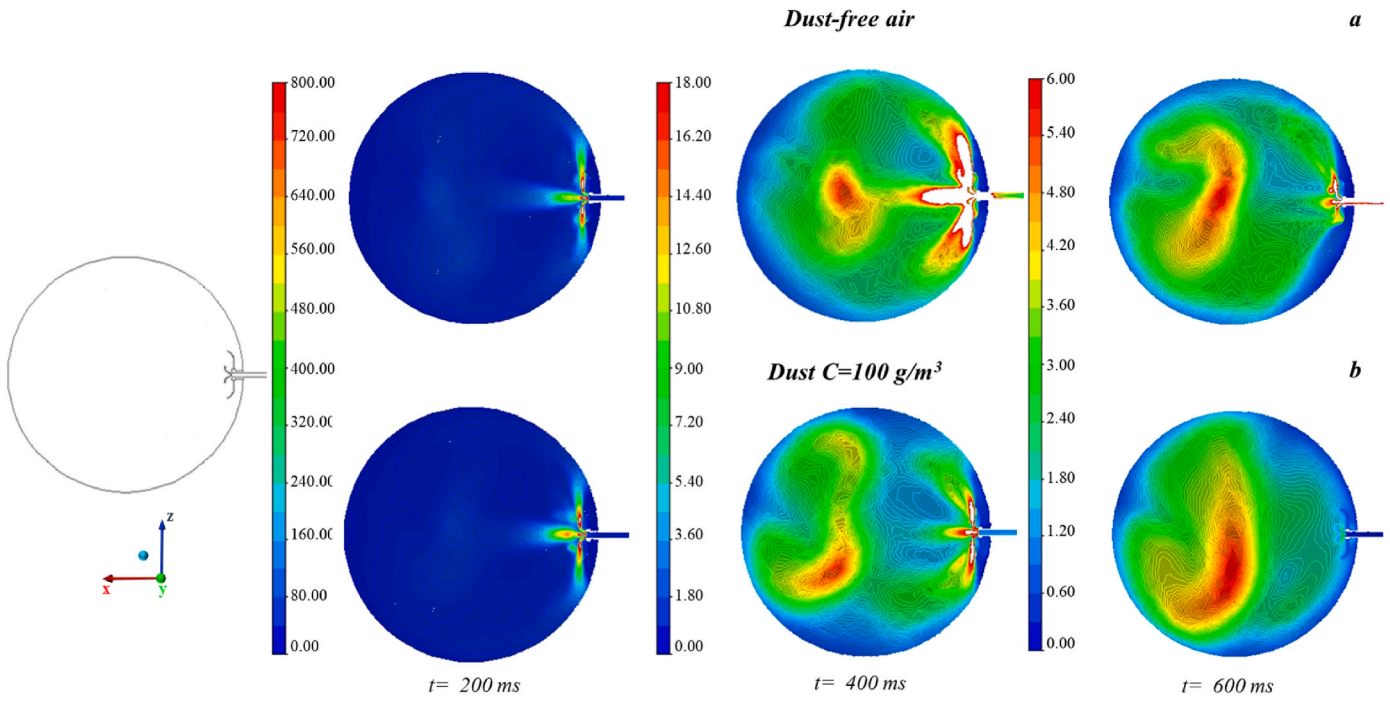

Fig. 5. Time sequence of computed maps of turbulent kinetic energy (m^2/s^2): dust-free air (a) and dust C = 100 g/m^3 (b), (x–z) plane, rebound nozzle.

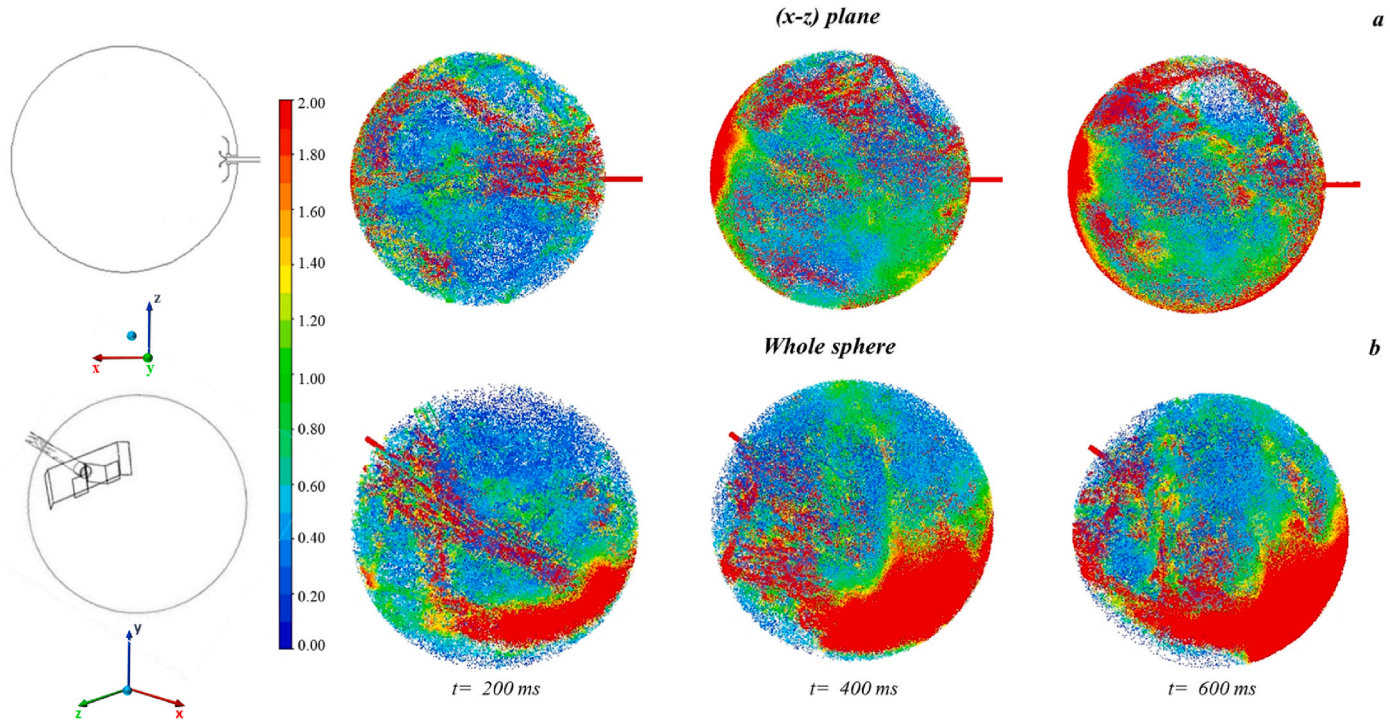

Fig. 6. Time sequence of particle tracks coloured by χ: (x–z) plane (a) and whole sphere (b), dust C = 100 g/m^3, rebound nozzle.

In Fig. 7 the time sequence of the turbulent kinetic energy maps is shown as computed over the (x-z) plane for the 1 m^3 vessel equipped with rebound nozzle (a) and perforated annular nozzle (b). At all times, the turbulent kinetic energy computed in the 1 m^3 vessel equipped with rebound nozzle is higher and less uniform than the one found with perforated annular nozzle. Indeed, at the ignition delay time (600 ms), the former has a maximum turbulent kinetic energy (in the centre) equal to 4.5 m^2/s^2, while the latter has a very narrow variation range of turbulent kinetic energy from the centre to the wall (from 1.25 m^2/s^2 to 0 m^2/s^2) (Portarapillo et al., 2020b). Fig. 8 shows the temporal trend of the RMS velocity as computed in the centre of the vessels as a function of time. The experimental data measured by Dyduch et al. (2016) for the rebound nozzle and by Hauert and Vogl (1995) for the perforated annular nozzle (Dyduch et al., 2016; Hauert and Vogl, 1995) are reported for the sake of comparison. At each time in the ignition point, the vessels show values of turbulent kinetic energy very different from each other. In particular, the turbulent kinetic energy is always higher in the case of the rebound nozzle than for the perforated annular one. The

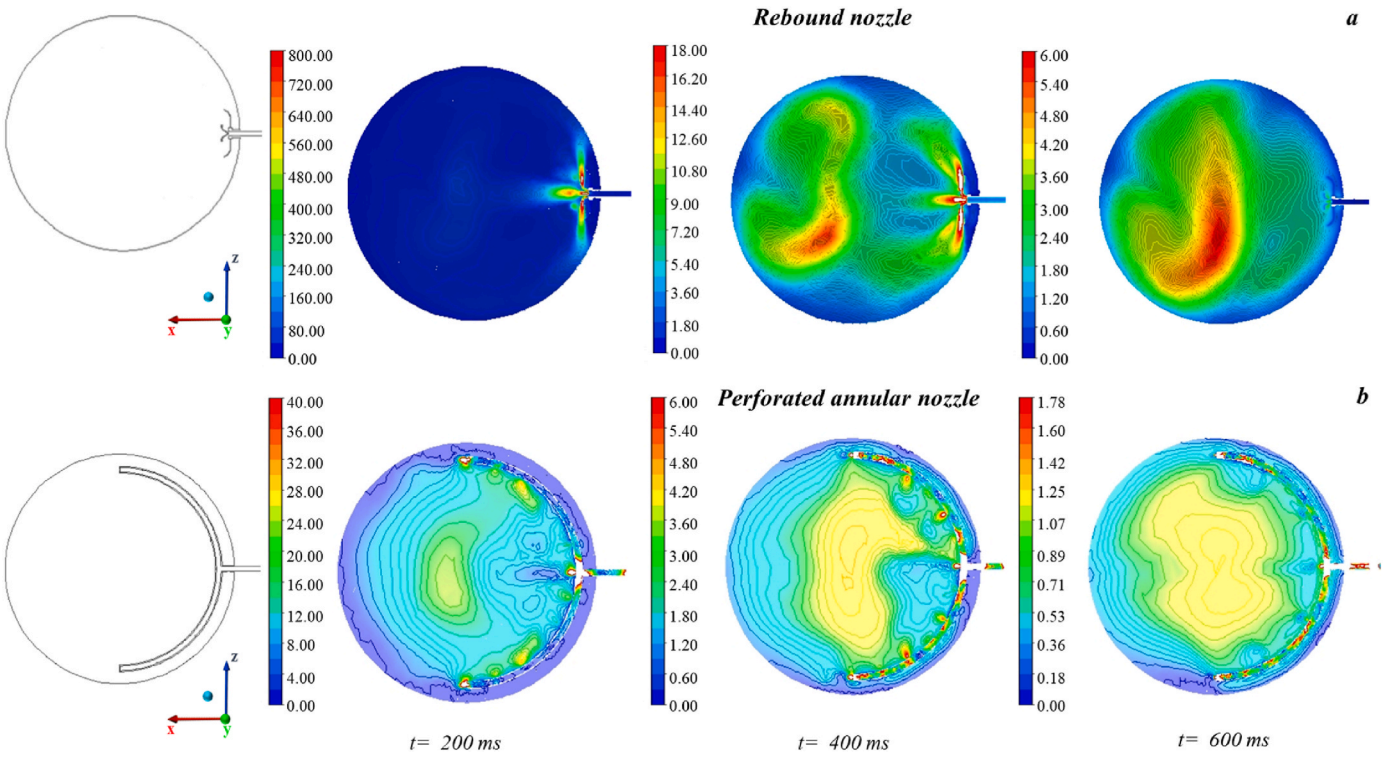

Fig. 7. Time sequence of turbulent kinetic energy maps (m^2/s^2): rebound nozzle (a) and perforated annular nozzle (b) ((x–z) plane), dust C = 100 g/m.[3].

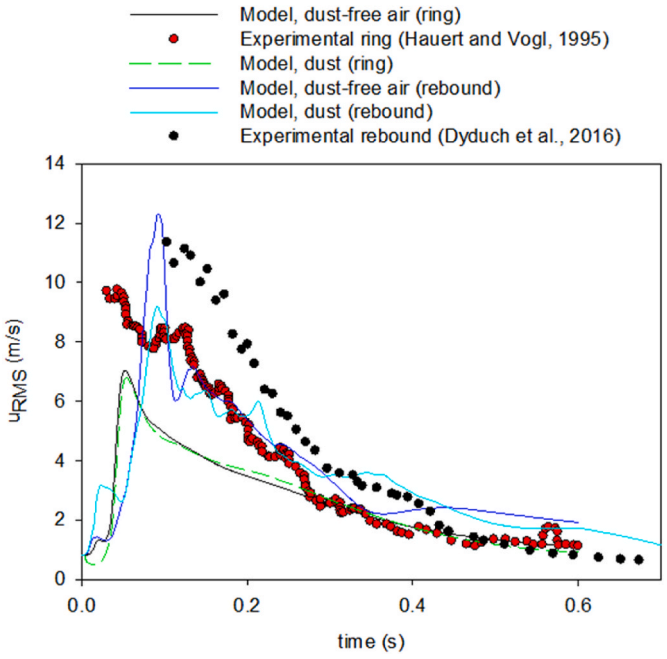

Fig. 8. *– RMS turbulence velocity (m/s) as a function of the time at the centre of the 1 m^3 vessel for dust free air (black and blue lines for ring and rebound nozzles, respectively) and dust-air mixture (green dash and cyan lines for ring and rebound nozzles, respectively). Literature data are also shown for comparison (black scatter plot* (Dyduch et al., 2016) *and red scatter plot* (Hauert and Vogl, 1995)*).* (For interpretation of the references to colour in this figure legend, the reader is referred to the Web version of this article.)

experimental data measured for both nozzles reach the same plateau value of 1.25 m^2/s^2 starting from 0.45 s, while the data deriving from the model with rebound nozzle (cyan line) are always higher. From these data, we conclude that to achieve a comparable turbulence level within the vessel, the ignition delay time may be increased in the case of rebound nozzle. According to standards, the recommended ignition delay time for the 1 m^3 vessel is equal to (600 ± 100) ms and in the case of rebound nozzle, the calibrated condition in the case of fibrous dust are 700 ms as ignition delay time (Sattar et al., 2016). Following the cyan line in Fig. 8 up to 700 ms, a reduction in terms of turbulent kinetic energy can be seen reaching a value of 1.3 m^2/s^2.

Fig. 9 shows the spatial-temporal distribution of dust concentration inside the sphere represented through the ratio χ for the 1 m^3 vessel equipped with rebound nozzle (a) and perforated annular nozzle (b). At ignition, the vessels show particle distributions very different from each other. Starting from 400 ms, in the case of perforated annular nozzle, the dust creates a three-dimensional cross inside the vessel. Conversely, in the case of rebound nozzle, no three-dimensional cross can be seen, and the dust distribution is characterized by an accumulation of dust in the centre and at the bottom of the sphere due to the gravity influence. In both cases, at the ignition time (t = 600 ms), the cloud is not uniform, suggesting that the flame will start propagating in a stratified flammable mixture, eventually leading to K_{St} values very different.

Fig. 10 shows the temporal trend of the DPM concentration as computed in the centre of the vessels as a function time. The experimental data measured by Hauert and Vogl (1995) for the perforated annular nozzle are reported for the sake of comparison (Hauert and Vogl, 1995). At the best of our knowledge, no experimental data about dust concentration in the centre of the 1 m^3 vessel equipped with rebound nozzle are available. As can be seen, the concentration of the dust in the case of rebound is always higher than in the case of perforated annular nozzle due to the vortices generation and the dust accumulation on their edges. Extending the ignition delay time up to 700 ms, the turbulence dissipation corresponds to a reduction in the concentration at the centre of the sphere, with a more uniform condition in the core of the sphere but a greater accumulation on the bottom due to gravity.

The huge difference between the dust concentration at the centre in the case of rebound and annular nozzles, suggest that the evaluation of

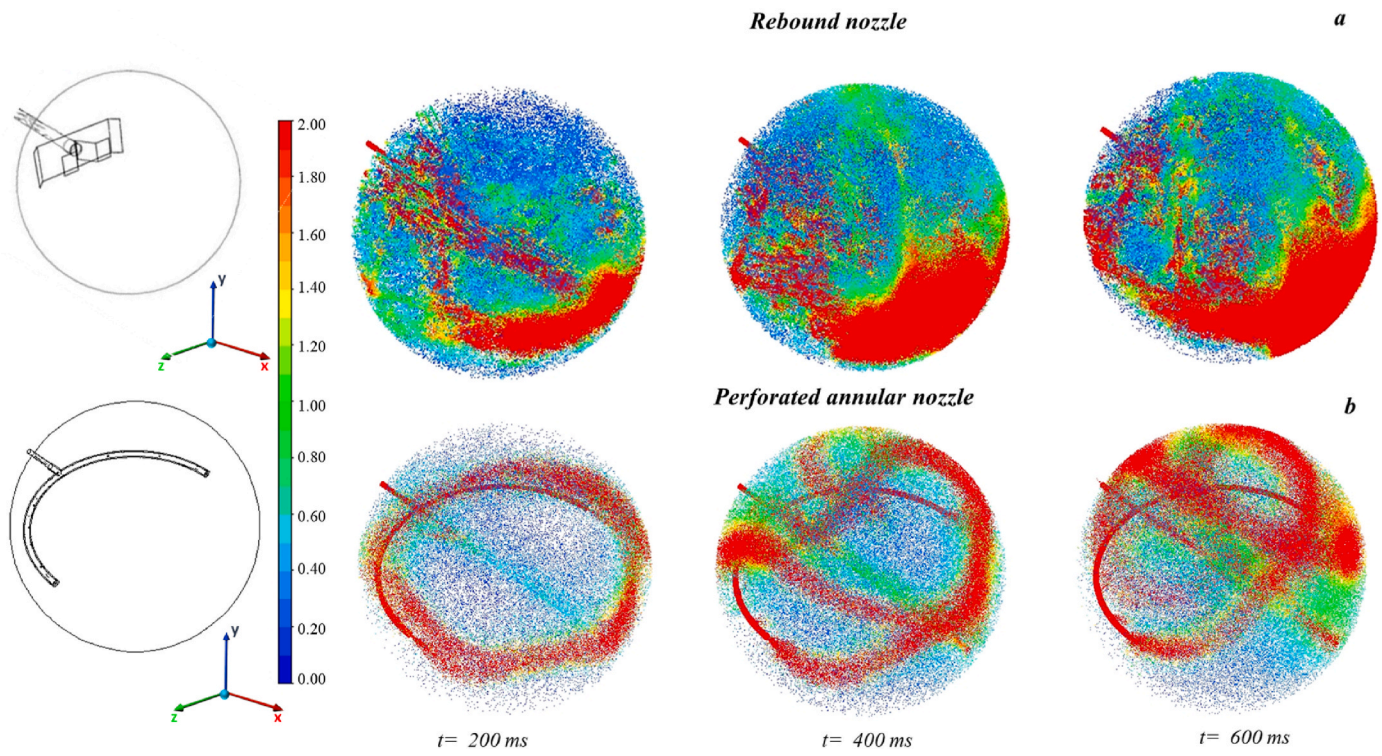

Fig. 9. Time sequence of particle tracks coloured by χ computed in the whole spheres: rebound nozzle (a) and perforated annular nozzle (b) ((x–z) plane), dust C = 100 g/m.^{3}.

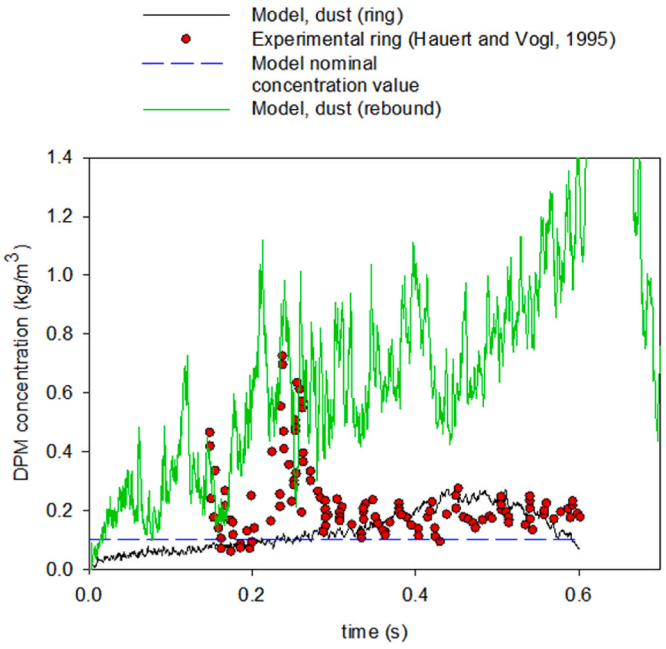

Fig. 10. – *DPM concentration as computed in the centre of the spheres for perforated annular (black line) and rebound (green line) nozzles as a function of time. Nominal concentration value* 100 g/m^3 *(dotted blue line) and literature data are also shown for comparison (red scatter plot* (Hauert and Vogl, 1995)*).* (For interpretation of the references to colour in this figure legend, the reader is referred to the Web version of this article.)

explosion parameters may give significantly different results when using different nozzles.

3.4. Turbulent combustion regimes

In the presence of a flame propagation in a turbulent flow field, different interactions between turbulence and combustion reaction may occur: corrugated flamelet regime, distributed regimes, pocket regime (Poinsot and Veynante, 2005). Depending on the combustion regime, different flame propagation modes and then different flame propagation velocity establish. All these have a significant impact on the explosion severity and then on the deflagration index.

In a previous work, we quantified the effect of initial turbulence level on the theoretical evaluation of the deflagration index in the 20 L and the 1 m^3 vessels (Portarapillo et al., 2021a). As a main conclusion, we found that the difference between the explosion tests in the 20 L and 1 m^3 vessels are qualitative other than quantitative, being different not only the turbulent kinetic energy but also the turbulent combustion regime (Portarapillo et al., 2021a). Starting from the data obtained by our simulations, we evaluated the combustion regime by changing the nozzle (rebound, perforated annular) and the ignition delay time (Abdel-Gayed and Bradley, 1989; Borghi, 1985; Peters, 1986; Poinsot, 1990).

In Table 3 the values of all the parameters and dimensionless numbers are given. Once set a reasonable value for the flame laminar burning velocity S_l (e.g., 0.4 m/s) and for the flame thickness l_F (e.g., 1 mm) and obtained the turbulent kinetic energy k and the dissipation rate ε from the CFD computations in the centre of the vessels (i.e., maximum values of these variables), we calculated the Kolmogorov dissipation scale η (Kolmogorov, 1941), the turbulent Karlovitz Ka and Reynolds Re numbers and the ratios u'/S_l and l/l_F. Results show that, although in the case of the rebound at 600 ms the initial turbulence level is higher than in the case with the ring, the larger dimensions of the vessel studied (compared to that of 20 L on a laboratory scale) entail a lower and uniform level of turbulence and corrugated type flame structure. By

Table 3
Numbers of the Borghi diagram as calculated for all the configuration.

	S_l [m/s] (max)	l_F [m]	k [m^2/s^2] (centre)	ε [m^2/s^3] (centre)	u' [m/s] (centre)	η [m]	u'/S_l	l/l_F	Ka	Re	Turbulent flame regime
1 m^3 rebound (600 ms)	0.4	1.00E-03	4.5	60	1.7	8.66E-5	4.3	623	0.36	4330	corrugated flamelets
1 m^3 rebound (700 ms)	0.4	1.00E-03	1.3	40	0.9	9.58E-5	2.3	623	0.14	2236	corrugated flamelets
1 m^3 perforated (600 ms)	0.4	1.00E-03	1.2	6	0.8	1.54E-4	2.2	623	0.13	2327	corrugated flamelets

increasing the ignition delay time of the rebound case, the velocity field becomes more similar to that found in the case of the ring. It is worth noting that in the case of rebound at 600 ms the Kolmogorov length scale is more similar to the corresponding flame thickness compared to the other cases. Thus, the case of rebound at 600 ms is closer to the transition line between corrugated flamelets and thin reaction zone regimes in the Borghi diagram (Borghi, 1985). In conclusion, the greatest effect on the initial level of turbulence and turbulent combustion regime is exerted by the size of the vessel and not by the nozzle used.

4. Conclusions

CFD simulations allow the quantification of the temporal/spatial profiles of turbulent kinetic energy and dust concentration in the 1 m^3 vessel equipped with rebound nozzle. The computed turbulent kinetic energy and dust concentration were validated against the available experimental data (at times higher than 300 ms). Although the level of turbulence is not completely uniform within the sphere at 600 ms, showing a decay moving from the centre to the walls, the variation range of turbulent kinetic energy is very narrow (from 4.5 m^2/s^2 to 0 m^2/s^2). Conversely, the dust is mainly concentrated at the outer zones of the vortices generated in the vessel and then dust concentration is not uniform. Comparison with the turbulent kinetic energy in the 1 m^3 vessel equipped with perforated annular nozzle, shows that the turbulence level in the case of the rebound is higher, as the amount of dust effectively fed into the vessel. However, checking the turbulent combustion regime established in the 1 m^3 vessel equipped with different nozzles, it is clear that the greatest effect on the initial level of turbulence and turbulent combustion regime is exerted by the size of the vessel rather than by the nozzle used. Further simulations are in progress to quantify the effect of the properties of the dust on the dispersion obtained in this vessel equipped with the rebound nozzle, which due to the partial feeding obtained with the perforated annular nozzle, is currently widely used also for spherical dusts. In particular, attention will be focused on the effect of the properties on the sedimentation phenomenon.

Credit author statement

Maria Portarapillo: Methodology; Investigation; Writing – original draft. Marco Trofa: Methodology, Writing – review & editing. Roberto Sanchirico: Writing – review & editing. Almerinda Di Benedetto: Conceptualization; Writing – original draft; Supervision

Declaration of competing interest

The authors declare that they have no known competing financial interests or personal relationships that could have appeared to influence the work reported in this paper.

References

Abdel-Gayed, R.G., Bradley, D., 1989. Combustion regimes and the straining of turbulent premixed flames. Combust. Flame 76, 213–218. https://doi.org/10.1163/187529293X00358.

ASTM E1226-19, 2019. Standard Test Method for Explosibility of Dust Clouds. ASTM Int, West Conshohocken, PA, pp. 1–15. https://doi.org/10.1520/E1226-19.

ASTM E1515-14, 1993. Standard Test Method for Minimum Explosible Concentration of Combustible Dusts 1. ASTM Int, West Conshohocken, PA, pp. 1–9. https://doi.org/10.1520/E1515-14.

ASTM E2931-13, 2013. Standard Test Method for Limiting Oxygen (Oxidant) Concentration of Combustible. ASTM Int, West Conshohocken, PA. https://doi.org/10.1520/E2931–13.

Borghi, R., 1985. On the structure and morphology of turbulent premixed flames. In: Recent Advances in the Aerospace Sciences, pp. 117–138.

BS EN 14034–1, 2004. Determination of Explosion Characteristics of Dust Clouds Part 1: Determination of Maximum Pressure Pmax of Dust Clouds 3.

Cashdollar, K.L., Chatrathi, K., 1992. Minimum explosible dust concentrations measured in 20-L and 1-M3 chambers. Combust. Sci. Technol. 87, 157–171. https://doi.org/10.1080/00102209208947213.

Clouthier, M.P., Taveau, J.R., Dastidar, A.G., Morrison, L.S., Zalosh, R.G., Ripley, R.C., Khan, F.I., Amyotte, P.R., 2019. Iron and aluminum powder explosibility in 20-L and 1-m3 chambers. J. Loss Prev. Process. Ind. 62, 103927. https://doi.org/10.1016/J.JLP.2019.103927.

Di Benedetto, A., Russo, P., Sanchirico, R., Di Sarli, V., 2013. CFD simulations of turbulent fluid flow and dust dispersion in the 20 liter explosion vessel. AIChE 59, 2485–2496. https://doi.org/10.1002/aic.

Di Sarli, V., Sanchirico, R., Russo, P., Di Benedetto, A., 2015. CFD modeling and simulation of turbulent fluid flow and dust dispersion in the 20-L explosion vessel equipped with the perforated annular nozzle. J. Loss Prev. Process. Ind. 38, 204–213. https://doi.org/10.1016/j.jlp.2015.09.015.

Dyduch, Z., Toman, A., Adamus, W., 2016. Measurements of turbulence intensity in the standard 1 m3 vessel. J. Loss Prev. Process. Ind. 40, 180–187. https://doi.org/10.1016/j.jlp.2015.12.019.

Elghobashi, S., 1994. On predicting particle-laden turbulent flows. Appl. Sci. Res. 52, 309–329. https://doi.org/10.1007/BF00936835.

Fluent Inc, 2016. Chapter 15 discrete phase modelling, section 4 laws for heat and mass exchange. ANSYS FLUENT User's Guid 1–170.

Going, J.E., Chatrathi, K., Cashdollar, K.L., 2000. Flammability limit measurements for dusts in 20-L and 1-m3 vessels. J. Loss Prev. Process. Ind. 13, 209–219. https://doi.org/10.1016/S0950-4230(99)00043-1.

Hauert, F., Vogl, A., 1995. Measurement of Dust Cloud Characteristics in Industrial Plants (Number: PL 910695).

ISO 6184-1:1985, 1985. Explosion Protection Systems, Part 1, Determination of Explosion Indices of Combustible Dusts in Air.

Kalejaiye, O., Amyotte, P.R., Pegg, M.J., Cashdollar, K.L., 2010. Effectiveness of dust dispersion in the 20-L Siwek chamber. J. Loss Prev. Process. Ind. 23, 46–59. https://doi.org/10.1016/j.jlp.2009.05.008.

Kartushinsky, A.I., Michaelides, E.E., Rudi, Y.A., Tisler, S.V., Shcheglov, I.N., 2011. Numerical simulation of three-dimensional gas-solid particle flow in a horizontal pipe. AIChE J. 57, 2977–2988. https://doi.org/10.1002/aic.12528.

Kolmogorov, A., 1941. The local structure of turbulence in incompressible viscous fluid for very large Reynolds' numbers. Dokl. Akad. Nauk SSSR 30, 301–305.

Launder, B.E., Spalding, D.B., 1972. Lectures in Mathematical Models of Turbulence. Academic Press, London; New York.

Morsi, S.A., Alexander, A.J., 1972. An investigation of particle trajectories in two-phase flow systems. J. Fluid Mech. 55, 193–208. https://doi.org/10.1017/S0022112072001806.

Peters, N., 1986. Laminar flamelet concepts in turbulent combustion. In: 21th Symposium International on Combustion, pp. 1231–1250.

Poinsot, T., Veynante, D., 2005. Theoretical and Numerical Combustion - Second Edition. Edwards.

Poinsot, T.J., 1990. Direct Simulation of Turbulent Combustion.

Portarapillo, M., Di Sarli, V., Sanchirico, R., Di Benedetto, A., 2020a. CFD simulation of the dispersion of binary dust mixtures in the 20 L vessel. J. Loss Prev. Process. Ind. 67, 104231. https://doi.org/10.1016/j.jlp.2020.104231.

Portarapillo, M., Sanchirico, R., Di Benedetto, A., 2021a. Effect of turbulence spatial distribution on the deflagration index: comparison between 20 L and 1 m3 vessels. J. Loss Prev. Process. Ind. 71 https://doi.org/10.1016/j.jlp.2021.104484.

Portarapillo, M., Trofa, M., Sanchirico, R., Di Benedetto, A., 2021b. CFD simulations of the effect of dust diameter on the dispersion in the 1 m3 explosion vessel. Chem. Eng. Trans 86.

Portarapillo, M., Trofa, M., Sanchirico, R., Di Benedetto, A., 2020b. CFD simulations of dust dispersion in the 1 m3 explosion vessel. J. Loss Prev. Process. Ind. 68, 104274 https://doi.org/10.1016/j.jlp.2020.104274.

Proust, C., Accorsi, A., Dupont, L., 2007. Measuring the violence of dust explosions with the "20 l sphere" and with the standard "ISO 1 m3 vessel". Systematic comparison and analysis of the discrepancies. J. Loss Prev. Process. Ind. 20, 599–606. https://doi.org/10.1016/j.jlp.2007.04.032.

Rodgers, S.A., Ural, E.A., 2011. Practical issues with marginally explosible dusts—evaluating the real hazard. Process Saf. Prog. 30, 266–279. https://doi.org/10.1002/prs.

Sattar, H., Huescar-Medina, C., Slatter, D., Andrews, G.E., Phylaktou, H.N., Gibbs, B.M., 2016. Calibration of new dust dispersion systems in the 1m 3 standard dust explosion vessel for fibrous biomass testing. In: Proceedings of the 11th International Symposium on Hazards, Prevention and Mitigation of Industrial Explosions, 11th ISHPMIE.

Taveau, J.R., Lemkowitz, S.M., Hochgreb, S., Roekaerts, D., 2018. Scaling up metal dusts deflagrations severity. In: Proceedings of the Twelfth International Symposium on Hazards, Prevention, and Mitigation of Industrial Explosions. Soesterberg, Netherlands.

Taveau, J.R., Lemkowitz, S.M., Hochgreb, S., Roekaerts, D.J.E.M., 2019. Metal dusts explosion hazards and protection. Chem. Eng. Trans. 77, 7–12. https://doi.org/10.3303/CET1977002.

UNI EN 14034-(1–4), 2011. Determinazione delle caratteristiche di esplosione di nubi di polvere.